Surface forces between colloidal particles at high hydrostatic pressure

D. W. Pilat, B. Pouligny, A. Best, T. A. Nick, R. Berger, H.-J. Butt

Surface forces between colloidal particles at high hydrostatic pressure

D. W. Pilat,[1] B. Pouligny,[2] A. Best,[1] T. A. Nick,[1] R. Berger,[1,*] and H.-J. Butt[1]

[1]*Max Planck Institute for Polymer Research, Ackermannweg 10, 55128 Mainz, Germany*
[2]*Centre de Recherche Paul-Pascal, 115 Avenue Schweitzer, 33600 Pessac, France*

It was recently suggested that the electrostatic double-layer force between colloidal particles might weaken at high hydrostatic pressure encountered, for example, in deep seas or during oil recovery. We have addressed this issue by means of a specially designed optical trapping setup that allowed us to explore the interaction of a micrometer-sized glass bead and a solid glass wall in water at hydrostatic pressures of up to 1 kbar. The setup allowed us to measure the distance between bead and wall with a subnanometer resolution. We have determined the Debye lengths in water for salt concentrations of 0.1 and 1 m*M*. We found that in the pressure range from 1 bar to 1 kbar the maximum variation of the Debye lengths was <1 nm for both salt concentrations. Furthermore, the magnitude of the zeta potentials of the glass surfaces in water showed no dependency on pressure.

I. INTRODUCTION

Surface forces determine the stability, structure, and rheology of suspensions and emulsions, and are often present in environments with high hydrostatic pressure. Oceans are one example of an aqueous, high-pressure environment. With depths of up to 11 km, as in the case of the Mariana Trench, the hydrostatic pressure in oceans can reach up to 1.1 kbar. One important maritime system where the stability is governed by surface forces is colloidal organic carbon, which is "one of the largest reservoirs of organic carbon on the planet" [1]. Wells and Goldberg, for example, found that the removal of colloidal organic carbon from bulk sea water at a depth of up to 5 km mainly takes place by aggregation into larger colloids and subsequent sedimentation to the sea floor [2]. From the structure of colloidal organic carbon aggregates, these authors concluded that there is a repulsive force between the particles that must be overcome before aggregates can be formed. Surface forces at high hydrostatic pressure are also found in oil recovery. The rheology of water-based drilling muds at high pressure has been under investigation for more than two decades [3]. The rheology of suspensions is determined by interactions between individual particles [4]. To understand the rheology of suspensions at high pressures, surface forces between the suspended particles, e.g., charged, micron-sized clay platelets, need to be investigated.

Various methods have been used to measure surface forces, such as the surface-force apparatus [5,6], the colloidal probe technique [7,8], and optical trapping or total internal reflection microscopy [9–11]. These methods can quantify surface forces between different materials, under different conditions and at different temperatures. Measurements of surface forces at a hydrostatic pressure of up to 170 bars have been reported by Schurtenberger and Heuberger [12,13], who measured the force between two mica surfaces in carbon dioxide with an extended surface-force apparatus. They investigated the critical Casimir effect along the supercritical ridge of carbon dioxide [13].

One fundamental surface force in an aqueous electrolyte is the electrostatic double-layer force. This is of interest because most surfaces are charged in water, e.g., the surfaces of colloidal organic carbon particles and clay platelets [1,3,14,15]. The double-layer force determines the stability of many aqueous suspensions. Between a sphere and a plane with the same charge density σ and for distances much larger than the Debye length λ_D, the double-layer force can be approximated by [8,14,16]

$$F_{DL} = \frac{4\pi\lambda_D R\sigma^2}{\epsilon_0\epsilon}\exp\left(-\frac{D}{\lambda_D}\right) = F_0\exp\left(-\frac{D}{\lambda_D}\right). \quad (1)$$

Here, R is the radius of the sphere; ϵ_0 and ϵ are the vacuum permittivity and the dielectric constant of the medium between the surfaces, respectively. D is the shortest distance between the surface of the sphere and the plane. The Debye length can be calculated by [14]

$$\frac{1}{\lambda_D} = \sqrt{\frac{e^2}{\epsilon_0\epsilon k_B T}\sum_i c_i Z_i^2}. \quad (2)$$

Here, e is the elementary charge; k_B and T are the Boltzmann constant and the temperature in units of K, respectively. c_i and Z_i are the concentration and valency of the ith ion sort. Equation (1) may be related to the surface potential ψ_0 by using the linearized Grahame equation $\sigma = \frac{\epsilon\epsilon_0\psi_0}{\lambda_D}$ [14].

The double-layer force is well understood and characterized at ambient pressure, but has never directly been measured at high hydrostatic pressure. The effect of hydrostatic pressure on the double-layer force between colloidal particles in hydrothermal water is controversial [17–19]. It has been reported that the magnitude of the zeta potential of quartz in an aqueous NaCl solution (concentration 0.01 *M*) at $p\mathrm{H} = 4$ decreased by a factor of 5 when the hydrostatic pressure was increased from 1 to 4 bars [20]. Such a decrease in the zeta potential with increasing pressure was also hypothesized in order to explain the thickening behavior of an Aerosil silica suspension at a pressure of up to 150 bars [21]. A decrease in the zeta potential indicates a decrease in the surface potential ψ_0 and would thus decrease the amplitude F_0 of the double-layer force. In addition, the dielectric constant of water ϵ depends weakly on the hydrostatic pressure: It increases from

*berger@mpip-mainz.mpg.de

$\epsilon = 78$ at 1 bar to $\epsilon = 82$ at 1 kbar [22] ($T = 25\,^{\circ}$C). Thus, for an increase of the hydrostatic pressure from 1 bar to 1 kbar, an increase of λ_D and a change of F_0 by approximately 2.5% are expected [Eq. (2)].

In this article we report on the measurements of surface forces in aqueous electrolytes at a hydrostatic pressure of up to 1 kbar using an optical trapping method. Our aim is to elucidate the pressure dependency of the double-layer force in aqueous solutions at room temperature.

II. MATERIALS AND METHOD

Bowman *et al.* measured the bulk viscosity of water at a hydrostatic pressure of up to 13 kbars by means of optically trapping a glass bead, thus demonstrating that optical trapping at high hydrostatic pressure works effectively [23]. To achieve force measurements at high hydrostatic pressures, we developed a long-working-distance optical trapping method based on a method reported by Nadal *et al.* [24]. We performed force-distance measurements (force curves) inside an optical high-pressure cell between a colloidal glass bead and the upper inner wall of a rectangular glass capillary in aqueous NaCl solutions [Fig. 1(a)].

A. The optical setup

A long-working-distance (WD) optical trap, an interferometer, and an inverse optical microscope compose the optical setup [Fig. 1(b)]. The trapping laser (Laser Quantum, Finesse pure) was a diode-pumped solid-state laser that provided linearly polarized light at a wavelength of $\lambda = 532$ nm with a Gaussian beam profile at a laser power of 3 W. The power of the trapping beam was attenuated by combining a motorized $\frac{\lambda}{2}$ plate and a polarization-sensitive beam-splitter cube (Workshop of Photonics, Motorized Standard Watt Pilot, high-power version). The rotation of the $\frac{\lambda}{2}$ plate and thus the attenuation were controlled by a computer. A second pair of a fixed $\frac{\lambda}{2}$ plate and a polarization-sensitive beam-splitter cube split the trapping beam with a power ratio of 1:2. The trapping beam was thus limited to a maximum power of 1 W. The power of the trapping beam after exiting the fixed attenuator (P_{Laser}) was monitored for all experiments. The power splitter (also a motorized standard Watt Pilot) split the trapping laser into two perpendicularly polarized beams with an adjustable power ratio. The downwards trapping beam was directed into the condenser (Nikon, 50 ×, NA = 0.4, WD = 22 mm) and the upwards trapping beam into the objective (Nikon, 50 ×, NA = 0.6, WD = 11 mm) with both foci overlapping inside the high-pressure cell (HPDS High Pressure Cell [25]). The space between the objective and the condenser was >3cm, which was large enough to mount the high-pressure cell in between. The high-pressure cell was clamped onto a platform connected to a motorized translation stage (Vision Lasertechnik), allowing the cell to be moved relative to the foci of the trapping beams. Furthermore, both trapping beams could be blocked by computer-controlled shutters. Measurement of the radii of the beam waists of both trapping beams inside the high-pressure cell resulted in $w_0 = 2.7 \pm 0.4\ \mu$m.

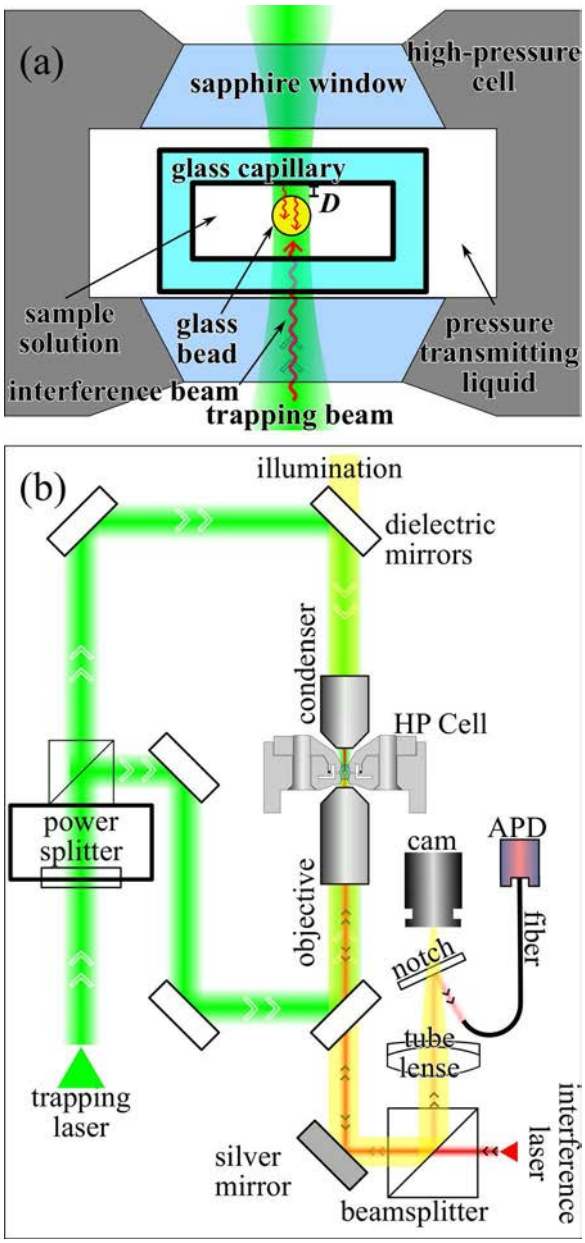

FIG. 1. (a) Surface-force measurement inside a high-pressure cell: The high-pressure cell allowed light to be transmitted through two sapphire windows (window thickness = 2.2 mm). The cell was filled with water that could be pressurized by a piston screw pump (not shown). A sealed rectangular glass capillary filled with the sample solution and the glass beads was placed inside the cell. A single glass bead was pushed against the upper wall of the glass capillary by a moderately focused trapping beam (green). The distance D was determined by measuring the interference between the reflection of a second laser beam (red) off the surface of the bead and the wall. (b) Optical trapping and interferometry setup for measurements inside a high-pressure cell: The components were mounted on a vertical optical breadboard. Thick green line: beam path of the trapping laser. Thin red line: Beam path of interference laser. Yellow: Light path of optical microscope. The drawing of the high-pressure cell (HP Cell) is based on the high-pressure cell described by Hartmann *et al.* [25] and a technical drawing provided by Andreas Zumbach (RECORD Maschinenbau GmbH, Königsee, Germany). APD: Avalanche photodiode.

In order to measure the bead-glass distance, we used an ultra-low noise laser-diode module (Coherent, ULN, 5 mW, $\lambda = 635$ nm). The high-power dielectric mirrors (CVI Melles Griot) reflected the light of the trapping laser and allowed the light of the interference laser to be (partially) transmitted. The interference laser was aligned on top of the trapping beam. The rays reflected off the surfaces of the bead and the wall interfered [Fig. 1(a)], and were guided into an avalanche photodiode (Thorlabs, APD130A/M) via a nonpolarizing beamsplitter cube, a notch filter (Thorlabs, wavelength of center = 633 nm, FWHM = 25 nm), and an optical fiber (Thorlabs, M69L01, core diameter = 300 μm, NA = 0.39). The notch filter was slightly tilted, shifting the reflected light to larger wavelengths, thus allowing a small part of the interference signal to enter the microscope camera. A similar optical setup for the same interferometry technique was published recently by Suraniti *et al.* [26]. The illumination, condenser, objective, tube lens, and camera formed an inverse optical microscope. Monitoring the reflected interference pattern at 635 nm together with the microscope image of a trapped bead allowed alignment of the interference laser. The optical fiber allowed for collection of the isolated on-axis interference signal. The intensity of the interference signal measured with the APD was recorded with a sampling rate of 50 kHz, thus fulfilling the Nyquist criterion as the fastest recorded frequency was of the order of 5 kHz.

B. Sample preparation

In order to realize defined aqueous sample solutions subject to high hydrostatic pressure, an 8-mm-long rectangular glass capillary (VitroCom, VitroTubes 5010-050, borosilicate rectangular glass capillary, nominal inner dimensions of cross section: 0.1 mm × 1 mm) was used as a capsule inside the high-pressure cell [Fig. 1(a)]. Two aqueous solutions of NaCl were prepared with concentrations of $c_0 = 0.10 \pm 0.01$ mM and $c_0 = 1.0 \pm 0.1$ mM. These low NaCl concentrations were chosen in order to avoid aggregation of particles or attachment to the walls. The Debye lengths were larger than 8 nm in both concentrations of NaCl. Due to this slow decay of the double-layer force, changes in the force of the order of 1 pN corresponded to changes in distance that could be well resolved. The solutions were prepared with ultrapure water provided by a Sartorius Arium 611 VF purification system (resistivity of 18.2 MΩ cm).

The glass beads were supplied as a dry powder (DUKE Scientific, 9000 Series, 8-µm-diameter borosilicate glass microspheres, Fig. 2). They were dispersed in ultrapure water and sonicated for at least 15 min. We mixed 1 ml of NaCl solution and 50 µl of the bead dispersion before filling the capillary, thus diluting the sample solutions to a salt concentration of $c_0 = 95 \pm 10$ μM and $c_0 = 0.95 \pm 0.1$ mM, respectively (concentration of beads <0.1 v/v %). The pH values of the samples were approximately pH = 4–4.5 (measured with MERCK pH-indicator strips Acilit). The capillary was filled with the sample solution by capillary rise, sealed by dipping the ends of the capillary into a pressure-transmitting sealing paste (Bayer, high-viscosity Baysilone paste), and placed in the middle of the high-pressure cell. Consequently, any exchange between the aqueous sample solution and the pressure-transmitting water was avoided. The high-pressure cell was then filled with water, closed, and connected to the high-pressure periphery consisting mainly of a piston screw pump (HiP, High Pressure Equipment Company) to pressurize the water with a maximum pressure of 1 kbar.

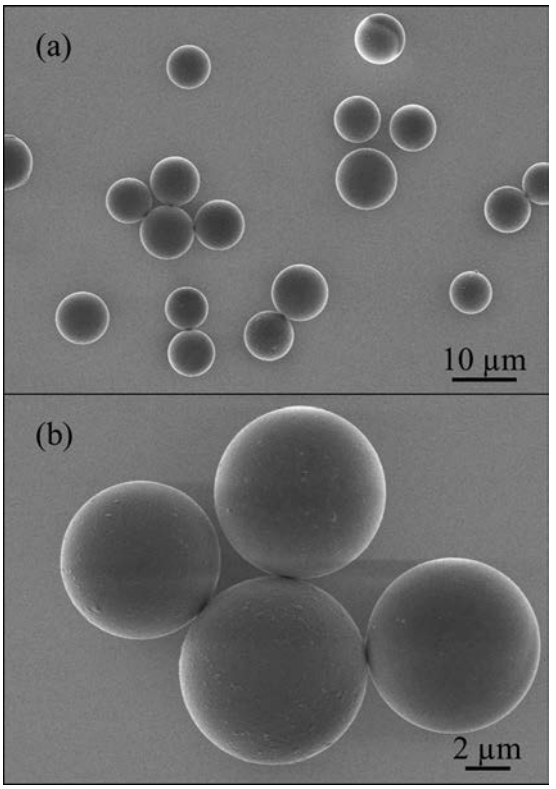

FIG. 2. Scanning electron microscopy images of the beads used here, shown at two different magnifications. Beads were supplied as a dry powder. For scanning electron microscopy imaging a small amount of the dry powder was poured onto a Si wafer coated with 20 nm of Pt. A 3-nm-thick layer of Pt was then sputtered onto the sample. (b) Closeup of (a).

C. Experimental procedure

Using optical microscopy, we selected a single bead for the experiment, trapped it at the lower wall of the capillary, and separated it from the other beads by moving the cell laterally. Then the bead was pushed upwards to the upper inner wall of the capillary, where the force curves were measured [Fig. 1(a)]. It is known that the radius, the roughness, and the surface charge density of a bead have an influence on the electrostatic double-layer force [Eq. (1)] [27]. Thus, in one experimental series the same bead was used to record all force curves at a given salt concentration. This procedure ensured comparability of the force curves recorded at different pressures.

Since the radiation pressure force acting on the bead (F_{RP}) is proportional to P_{Laser} [11], a force curve was recorded by stepwise increasing P_{Laser}. The force driving the bead against the wall is given by

$$F_{\mathrm{bead}} = -F_{\mathrm{RP}} + F_{\mathrm{G}} - F_{\mathrm{B}}. \tag{3}$$

Here, F_G and F_B are gravity and bouyancy, which were constant during the experimental procedure. Forces F_{RP} and F_B act in the opposite direction to F_{DL}, thus the negative sign. At each step of P_{Laser} (single measurement) the bead was pushed against the wall by the trapping beam [Fig. 1(a)]. Starting a few micrometers away from the wall, the bead moved against the wall. F_{bead} was determined from analysis of the bead's trajectory far from the wall ($D > 7\lambda_D$). Close to the wall, the bead reached an equilibrium distance D_{eq}, where the force pushing the bead against the wall was in equilibrium with the repulsive double-layer force, i.e., $F_{bead} = -F_{DL}(D_{eq})$. Evaluation of the bead's thermal motion yielded the value of D_{eq} [24]. The attenuation of the trapping beam and the data acquisition were computer controlled. Thus, a force curve consisting of 10–20 force-distance pairs was recorded automatically within 1–3 min.

D. Data analysis

The distance between bead and wall was determined by evaluating the reflected interference signal collected by the avalanche photodiode (I_{APD}). The intensity-distance relationship of the interference signal is given by [28]

$$2I_{APD} = I_{max} + I_{min} - (I_{max} - I_{min})\cos\left(\frac{4\pi n_1}{\lambda}D + \Phi\right). \tag{4}$$

The refractive index of water n_1 at hydrostatic pressure up to $P = 1$ kbar was previously determined by Schiebener *et al.* [29]. I_{max} and I_{min} are the intensities of a maximum and a minimum of the interference signal, and Φ is the phase of the cosine function upon contact of bead and wall. For consecutive extrema in the measured interference signal, the corresponding difference of D is $\Delta D = \frac{\lambda}{4n_1} \approx 119$ nm. The trajectory of the bead while moving towards the wall could thus be deduced by determining the temporal positions of the extrema in the interference signal (Fig. 3, blue empty squares). After the minimum at approximately 1.12 s in Fig. 3 the reflected interference signal was strictly monotonic in D; thus Eq. (4) could be inverted in order to determine D (Fig. 3, blue line).

At distances D between 0.2 and 3 µm (Fig. 3, left of 1.13 s), the double-layer force was negligible because for the here used salt concentrations $D > 7\lambda_D$. When the bead moved through the liquid, F_{bead} was counteracted by the hydrodynamic force F_H, given by

$$F_H = -6\pi R v \eta\left(1 + \frac{R}{D}\right). \tag{5}$$

Here, η is the dynamic viscosity of the liquid, and $v = dD/dt$ and R are the velocity and radius of the bead, respectively. Wall effects due to draining the liquid between the bead and the wall are considered by using the factor $(1 + R/D)$ [14], which is an approximation of the only numerically computable exact Brenner factor [30]. Owing to the moderate focusing of the trapping beam, the width of the beam increased by less than 0.3% at a distance of 3 µm from the beamwaist. Thus F_{RP} and consequently F_{bead} were considered to be constant during one single measurement.

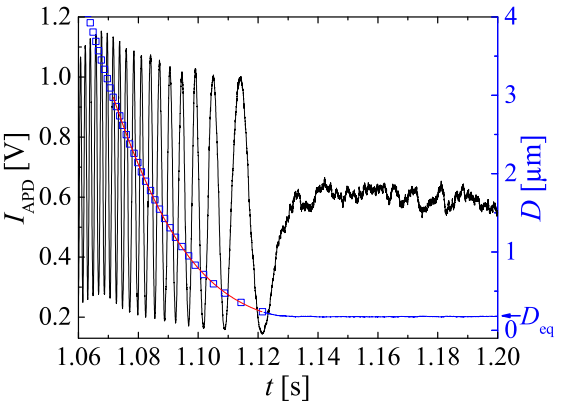

FIG. 3. Example of a bead pushed against the wall by the trapping beam with $P_{Laser} = 124$ mW. Black line and left axis: Intensity of the reflected interference signal I_{APD} between bead and wall versus time. Empty blue squares, blue line, and right axis: Trajectory of the bead. D is the absolute distance of the bead and the upper inner wall of the glass capillary [Eq. (4)]. At times >1.13 s the bead showed thermal motion around the distance D_{eq} where $F_{bead} = -F_{DL}(D_{eq})$. In this case, we measured $D_{eq} = 176.4 \pm 0.9$ nm and $F_{bead} = 19.6 \pm 0.3$ pN. The error of the absolute force value was 22% and arose mainly from the error in determining the bead radii $\Delta R = 0.5\,\mu$m due to the resolution of the microscope. The red line is a fit on the interval [0.2 µm, 3 µm] with Eq. (5). We notice an envelope of the cosine signal in the measured intensity signal that is not accounted for by Eq. (4). This envelope is due to a lensing effect of the bead.

With our setup it is possible to measure relative distances $\tilde{D} = D + D_0$, where D_0 is an offset. Thus, the absolute distance D is not known *a priori*. For the calculation we defined $\tilde{D} := 0$ being the position corresponding to the last extremum of the measured intensity in a single measurement (Fig. 3, approximately at 1.12 s). Solving Eq. (5) and substituting $D = \tilde{D} - D_0$ yielded the implicit solution for the bead's trajectory,

$$t - t_0 = -\frac{6\pi\eta}{F_H}[R(\tilde{D} - D_0) + R^2 \ln(\tilde{D} - D_0)], \tag{6}$$

which was used to fit the trajectory of the bead during laser-driven sedimentation starting from a bead-wall distance of 3 µm (Fig. 3, red line). Values for the viscosity of water were taken from the NIST Chemistry WebBook [31]. From this model we derived F_{bead} as $F_H = -F_{bead}$, and D_0. For the measurement shown in Fig. 3 we obtained $F_{bead} = 19.6 \pm 0.3$ pN and $D_0 = -216 \pm 5$ nm. D_0 is identical for all single measurements belonging to one force curve. For the force curve recorded at ambient pressure and a NaCl concentration of 0.1 mM in water (Fig. 4), we found a mean value of $D_0 = -202 \pm 15$ nm, where the uncertainty is the standard deviation.

The refractive indices of the glass beads and the glass wall were higher than the refractive index of water. Thus, the phase of the cosine function in Eq. (4) is defined and becomes $\phi = \pi$ [32]. Consequently, D_0 can only assume values that are multiples of $-\frac{\lambda}{2n}$ and we can, therefore, conclude that the absolute distance between the bead and wall was $D = \tilde{D} + \frac{\lambda}{2n} \approx \tilde{D} + 238$ nm. We attribute the difference between the measured value of D_0 (i.e., -202 ± 15 nm) and

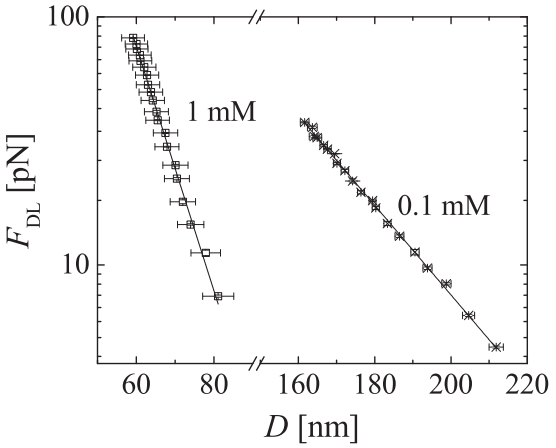

FIG. 4. Surface force versus distance at ambient pressure for NaCl concentrations of 0.1 and 1 mM in water: pH = 4–4.5, $T = 21 \pm 1\,^{\circ}$C. By increasing P_{Laser} with every single measurement, we increased F_{bead} in equidistant steps of approximately 1.6 pN from 4.7 to 37.6 pN for 0.1 mM and in steps of approximately 3.7 pN from 7.5 to 82.2 pN for 1 mM. Solid lines represent fits with Eq. (1). At 0.1 mM the obtained fit values were $\lambda_{\text{D}} = 24.0 \pm 0.3$ nm and $F_0 = 31 \pm 3$ nN and at 1 mM $\lambda_{\text{D}} = 8.8 \pm 0.2$ nm and $F_0 = 69 \pm 9$ nN. The uncertainties of force values were 22% at 0.1 mM and 25% at 1 mM and arose mainly from the error in determining the bead radii due to the resolution of the optical microscope ($\Delta R = 0.5\,\mu$m).

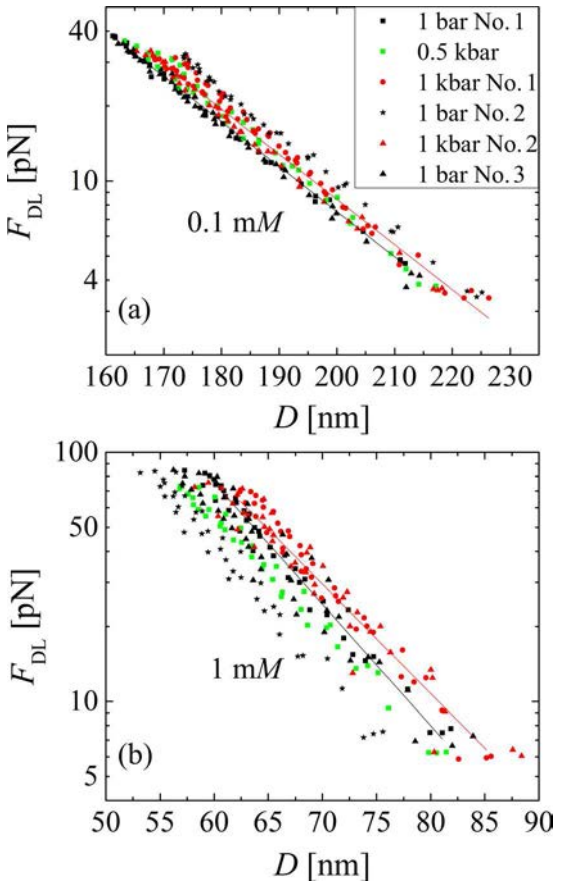

FIG. 5. Force measurement at pressures of 1 bar, 0.5 kbar, and 1 kbar for a concentration of (a) 0.1 mM and (b) 1 mM NaCl in water: All measurements at the same salt concentration were performed using the same sample liquid and the same bead ($T = 21 \pm 1\,^{\circ}$C). The experimental procedure was to measure in succession at pressures of 1 bar, 0.5 kbar, 1 kbar, 1 bar, 1 kbar, and finally at 1 bar. Results are plotted without error bars for better readability. Errors of single data points were accounted for by the fitting algorithm. The black and red lines are exemplary fits by Eq. (1) of the first force curve recorded at 1 bar and 1 kbar, respectively.

$-\frac{\lambda}{2n} \approx -238$ nm to the approximation of the Brenner factor and the uncertainty of the radius of the bead [Eq. (5)].

In order to determine D_{eq}, a histogram of distances D was determined for a 2-s-long interval of the bead's thermal motion around equilibrium. The probability density is highest for D_{eq} [33]. Thus, by determining the position of the maximum of the histogram we ascertained D_{eq}. It was found by Roichman *et al.* that fluctuations of the position of the bead lateral to the beam axis influence the mean axial position of the bead [34]. However, we have found that this effect is negligible in the case of our experimental configuration (see Appendix).

III. RESULTS AND DISCUSSIONS

Measurements as shown in Fig. 3 at stepwise increasing P_{Laser} provided pairs of F_{bead} and D_{eq} which together composed a force curve (Fig. 4). In a semilogarithmic plot, the force curves are linear, showing the exponential behavior as expected for the double-layer force [Eq. (1)]. The force decayed more steeply in the 1 mM NaCl salt concentration than in the 0.1 mM concentration, owing to additional ions screening the electrostatic field. Consequently, at higher salt concentrations, the equilibrium distance of the bead was closer to the glass wall. We fitted the force curves with Eq. (1) using orthogonal regression. The fit revealed $\lambda_{\text{D}} = 24.0 \pm 0.3$ nm and $\lambda_{\text{D}} = 8.8 \pm 0.2$ nm at 0.1 mM and 1 mM NaCl concentrations, respectively. These values agree with the theoretically predicted Debye lengths of $\lambda_{\text{D}} = 24.2-30.1$ nm and $\lambda_{\text{D}} = 8.9-10.3$ nm [Eq. (2)]. Here the errors of salt concentration, pH, and temperature were taken into account. The resolution in distance measurement may best be observed in the force curve at 1 mM salt concentration for forces >53 pN (Fig. 4). At such forces, six distinguishable data points were recorded at distances D between 59 and 63 nm, thus demonstrating a subnanometer spatial resolution.

We performed several measurements at hydrostatic pressures of 1 bar, 0.5 kbar, and 1 kbar (Fig. 5), and measured at least three force curves consecutively at each pressure. Consecutive force curves at the same pressure are plotted with the same symbols (e.g., black squares in Fig. 5) and overlapped on average within 3% and 15% of their magnitude for the 0.1 mM and the 1 mM NaCl concentrations, respectively. For most consecutively measured force curves the values of λ_{D} varied by less than 1 nm for both salt concentrations.

For force curves that were not recorded consecutively, we observed an error that we attribute to the anisotropy of the beads. For example, at 0.1 mM NaCl concentration, the force curves of the first and last 1-bar measurements overlap within less than 4% of their magnitude (black squares and triangles). However, for the force curves of the second 1-bar measurement (black stars), the magnitude of the force

TABLE I. Averaged fit values of force curves recorded at different hydrostatic pressures (Fig. 5) fitted with Eq. (1).

c_0 (mM)	1 bar	0.5 kbar	1 kbar
0.1	λ_D (nm) = 23.3 ± 0.6	22.7 ± 0.3	22.5 ± 1.1
0.1	F_0 (nN) = 43 ± 9	53 ± 9	64 ± 30
1	λ_D (nm) = 9.0 ± 0.6	9.0 ± 0.4	9.5 ± 0.9
1	F_0 (nN) = 55 ± 26	43 ± 8	61 ± 40

apparently increased by approximately 40% compared to the first and last 1-bar measurements. A close inspection of the scanning electron micrographs revealed that the beads were not perfectly symmetrically shaped (Fig. 2). Furthermore, the beads may be inhomogeneous with respect to their optical density and surface charge. Charge inhomogeneity has been observed in measurements with polystyrene particles [35] and hypothesized for silica spheres [36]. Such inhomogeneity can influence the measured force values. Asymmetry in the bead's shape or optical density can cause preferred orientations during trapping. For example, the long axis of slightly elongated particles becomes locked in the direction of beam propagation during trapping [37]. When changing the pressure between measurements, the trapping laser had to be blocked for ≈5 min and thus the bead could change its orientation and lock into another orientation.

In case of the 0.1 mM NaCl concentration the magnitudes of the force curves measured at 0.5 kbar (green squares) and 1 kbar (red circles and triangles) were between the magnitudes of the force curves measured at 1 bar. In the case of the 1 mM NaCl concentration, the magnitudes of the force curves varied less for force curves at different pressures than for different force curves at 1 bar. Thus, within the statistical error, the force curves at high pressures showed no difference compared to those force curves recorded at ambient pressure. Nevertheless, we want to emphasize that the effect of the bead orientation does not influence the measured λ_D, which was found constant within approximately 1 nm at all hydrostatic pressures (Table I). Furthermore, F_0 values resulting from fitting of our data were not correlated with pressure (Table I).

IV. SUMMARY AND CONCLUSION

We have developed a method for measuring surface forces versus distance at hydrostatic pressures up to 1 kbar. A long-working-distance optical trap allowed glass beads to be trapped inside a high-pressure cell. Using the radiation pressure of the optical trap, we exerted forces up to 0.1 nN. The particle-wall distance was measured interferometrically with subnanometer resolution. We have demonstrated that our method allows quantitative analysis of surface forces.

The electrostatic double-layer force was measured directly at hydrostatic pressures of up to 1 kbar. Within the error of our experiment the Debye length was constant within less than 5% and within less than 10% when we increased the pressure from 1 bar to 1 kbar for aqueous solutions of 0.1 mM and 1 mM NaCl, respectively. We found no significant difference between force curves measured in the pressure range from 1 bar to 1 kbar. Of particular significance, we observed no change of the magnitude of the electrostatic double-layer force with increasing pressure within the error of our experiment. This demonstrates that the effect of pressure on the zeta potential is insignificant, which is contrary to previous findings [20,21]. Furthermore, no irreversible effects due to pressurization occurred. We can therefore conclude that the stability of aqueous dispersions at room temperature is not significantly influenced by hydrostatic pressure up to 1 kbar.

ACKNOWLEDGMENTS

We are grateful to Javed Ally, Günter Auernhammer, Alfons Becker, Helma Burg, Regina Fuchs, Achim Gerstenberg, Michael Kappl, Kaloian Koynov, Jean-Christophe Loudet, Günther Mauer, Besira Mihiretie, Maren Müller, François Nadal, Werner Steffen, Stefan Weber, and Andreas Zumbach for their support and fruitful discussions. Our thanks go to Fang Ren for providing calculations with his program ABSPHERE. D.W.P. is grateful for funding by the Studienstiftung des Deutschen Volkes. T.A.N. is grateful for the support of the Stiftung Rheinland Pfalz für Innovation 38 62 61/1071 and the Max Planck Graduate Center.

APPENDIX: INFLUENCE OF FLUCTUATIONS

The equilibrium position of the bead is determined by the balance between the optical force from the laser and the surface force between bead and wall. Strictly speaking, this problem pertains to statistical mechanics, because of the thermal fluctuations which make the particle explore a small volume around the "zero-temperature" position.

Roichman *et al.* (hereafter referred to as RSSG) have studied the effects of fluctuations on the position distribution of a bead trapped by optical tweezers [34]. These authors found that due to the nonconservative character of radiation pressure, the position of a bead executing thermal motion is not distributed around a steady equilibrium position, but traces out a toroidal vortex. This effect influences optical trapping experiments by

(1) increasing the width of the measured probability density of the bead's position, and

(2) shifting the mean equilibrium position of the bead.

In our experiments, the equilibrium distance D_{eq} was determined as the maximum of the measured probability density, assuming that $F_{bead} = -F_{DL}(D_{eq})$, with F_{bead} given by Eq. (3). A shift of the measured D_{eq} due to fluctuations could thus corrupt our force curves.

RSSG could explain their observations through a simple model of the force field (see the Supplemental Material with Ref. [34]):

$$\boldsymbol{F}(\boldsymbol{r}) = -k \exp\left(-\frac{r^2}{2\sigma^2}\right)\boldsymbol{r} + F_{RP} \exp\left(-\frac{r^2}{2\sigma^2}\right)\hat{\boldsymbol{z}}. \quad \text{(A1)}$$

Here $\boldsymbol{r}$ is the particle's position relative to the trap center, k and σ are the stiffness and the effective width of the trap, and F_{RP} is the strength of radiation pressure. In the zero-temperature limit, the particle's on-axis position is given by $z_{eq} = F_{RP}/k$. Using Eq. (43) of the Supplemental Material with Ref. [34] and assuming $k\sigma^2/(k_B T)$ to be very large, we get for the corrected

on-axis position

$$z^* \approx z_{\mathrm{eq}}\left(1 - \frac{2}{3}\frac{k_B T}{k\sigma^2}\right). \tag{A2}$$

Equation (A2) gives the amplitude of the position shift caused by fluctuations. De Meissieres *et al.* have introduced a simplified model that explained the findings of Roichmann *et al.* [38]. The force on an optically trapped bead was modeled as the sum of a harmonic restoring force and axial radiation pressure force,

$$\boldsymbol{F}(\boldsymbol{r}) = -k_x x\hat{x} - k_y y\hat{y} - k_z z\hat{z} + F_{\mathrm{RP}}^{\mathrm{eff}}(\rho)\hat{z}. \tag{A3}$$

Here k_i is the force gradient in the i direction and $\rho = \sqrt{x^2 + y^2}$ is the lateral displacement. This model may be applied to our experimental configuration. k_x and k_y are the lateral stiffnesses of our optical trap, which in good approximation can be assumed equal to each other, and k_z is the gradient of the electrostatic double-layer force $k_Z = \frac{dF}{dz}(D_{\mathrm{eq}})$. The effective radiation pressure force was modeled as a parabola,

$$F_{\mathrm{RP}}^{\mathrm{eff}}(\rho) = F_{\mathrm{RP}} + S\rho^2. \tag{A4}$$

Here F_{RP} is the on-axis radiation pressure force. For a bead that is large relative to the width of the trapping beam, as was the case in this work, S is positive. In the zero-temperature limit the lateral displacement of the bead would be zero and thus $F_{\mathrm{RP}}^{\mathrm{eff}}(0) = F_{\mathrm{RP}}$. However, at finite temperature lateral thermal motion will lead to an increase of $F_{\mathrm{RP}}^{\mathrm{eff}}$, thus changing the mean position in the z direction. We estimate the effect of lateral fluctuations through a corrected effective radiation pressure force given by

$$F_{\mathrm{RP}}^{\mathrm{eff}} \approx F_{\mathrm{RP}} + S\langle\rho^2\rangle = F_{\mathrm{RP}}\left(1 + \frac{S\langle\rho^2\rangle}{F_{\mathrm{RP}}}\right), \tag{A5}$$

with $\langle\rho^2\rangle = 2k_{\mathrm{B}}T/k_x$. From calculations based on the generalized Lorenz-Mie theory we get for our experimental configuration $k_x > 10^{-5}$ N/m and $S/F_{\mathrm{RP}} \approx 0.2\ \mu\mathrm{m}^{-2}$ [39,40], yielding

$$\frac{S\langle\rho^2\rangle}{F_{\mathrm{RP}}} = \frac{2Sk_{\mathrm{B}}T}{F_{\mathrm{RP}}k_{\mathrm{x}}} < 1.6 \times 10^{-4} \ll 1. \tag{A6}$$

The on-axis position is then

$$z^* = \frac{F_{\mathrm{RP}}^{\mathrm{eff}}}{k_{\mathrm{z}}} = z_{\mathrm{eq}}\left(1 + \frac{2Sk_{\mathrm{B}}T}{F_{\mathrm{RP}}k_{\mathrm{x}}}\right). \tag{A7}$$

The same approximation, when applied to RSSG model equation (A1) yields

$$z^* = z_{\mathrm{eq}}\left(1 - \frac{k_{\mathrm{B}}T}{\sigma^2 k_{\mathrm{x}}}\right). \tag{A8}$$

The latter result differs from the exact Eq. (A2) only by a factor of 2/3. The simple "thermodynamic correction" expressed by Eq. (A5) is then sufficient to conclude that the effect of fluctuations in our experiments can be safely disregarded.

[1] P. E. Kepkay, Mar. Ecol.: Prog. Ser. **109**, 293 (1994).
[2] M. L. Wells and E. D. Goldberg, Mar. Chem. **41**, 353 (1993).
[3] N. J. Alderman, A. Gavignet, D. Guillot, and G. C. Maitland, in *Proceedings of SPE Annual Technical Conference and Exhibition, Houston, Texas, 2–5 October 1988* (Society of Petroleum Engineers, Richardson, TX, 1988).
[4] Z. Zhou, P. J. Scales, and D. V. Boger, Chem. Eng. Sci. **56**, 2901 (2001).
[5] D. Tabor and R. H. S. Winterton, Proc. R. Soc. London, Ser. A **312**, 435 (1969).
[6] J. N. Israelachvili and D. Tabor, Proc. R. Soc. London, Ser. A **331**, 19 (1972).
[7] W. A. Ducker, T. J. Senden, and R. M. Pashley, Nature **353**, 239 (1991).
[8] H.-J. Butt, Biophys. J. **60**, 1438 (1991).
[9] D. C. Prieve, F. Luo, and F. Lanni, Faraday Discuss. **83**, 297 (1987).
[10] D. G. Grier, Curr. Opin. Colloid Interface Sci. **2**, 264 (1997).
[11] A. Ashkin, Phys. Rev. Lett. **24**, 156 (1970).
[12] E. Schurtenberger and M. Heuberger, Rev. Sci. Instrum. **82**, 103902 (2011).
[13] E. Schurtenberger and M. Heuberger, J. Supercrit. Fluids **71**, 120 (2012).
[14] H.-J. Butt and M. Kappl, *Surface and Interfacial Forces* (Wiley-VCH, Weinheim, 2010).
[15] J. N. Israelachvili, *Intermolecular and Surface Forces* (Elsevier Science, San Diego, CA, 2011).
[16] H. J. Butt, Nanotechnology **3**, 60 (1992).
[17] S. K. Ghosh and K. Tsujii, J. Phys. Chem. B **112**, 6906 (2008).
[18] S. Deguchi and S. A. Mukai, J. Phys. Chem. B **113**, 3251 (2009).
[19] S. K. Ghosh, J. Phys. Chem. B **113**, 3253 (2009).
[20] K. Rodríguez and M. Araujo, J. Colloid Interface Sci. **300**, 788 (2006).
[21] A. Amiri, G. Oye, and J. Sjoblom, Colloid Surf., A **378**, 14 (2011).
[22] M. Uematsu and E. U. Franck, J. Phys. Chem. Ref. Data **9**, 1291 (1980).
[23] R. W. Bowman, G. M. Gibson, M. J. Padgett, F. Saglimbeni, and R. Di Leonardo, Phys. Rev. Lett. **110**, 095902 (2013).
[24] F. Nadal, A. Dazzi, F. Argoul, and B. Pouligny, Appl. Phys. Lett. **79**, 3887 (2001).
[25] M. Hartmann, F. Pfeifer, G. Dornheim, and K. Sommer, Chem. Ing. Tech. **75**, 1763 (2003).
[26] E. Suraniti, F. Kanoufi, C. Gosse, X. Zhao, R. Dimova, B. Pouligny, and N. Sojic, Anal. Chem. **85**, 8902 (2013).
[27] Z. Gan, X. Xing, and Z. Xu, J. Chem. Phys. **137**, 034708 (2012).
[28] L. Limozin and K. Sengupta, ChemPhysChem **10**, 2752 (2009).
[29] P. Schiebener, J. Straub, J. M. H. Levelt Sengers, and J. S. Gallagher, J. Phys. Chem. Ref. Data **19**, 677 (1990).
[30] H. Brenner, Chem. Eng. Sci. **16**, 242 (1961).

[31] E. W. Lemmon, M. O. McLinden, and D. G. Friend, Thermophysical properties of fluid systems in *NIST Chemistry WebBook, NIST Standard Reference Database Number 69*, edited by P. J. Linstrom and W. G. Mallard (National Institute of Standards and Technology, Gaithersburg, MD, 20899); http://webbook.nist.gov (retrieved March 30, 2015).
[32] J. Radler and E. Sackmann, Langmuir **8**, 848 (1992).
[33] B. M. Alexander and D. C. Prieve, Langmuir **3**, 788 (1987).
[34] Y. Roichman, B. Sun, A. Stolarski, and D. G. Grier, Phys. Rev. Lett. **101**, 128301 (2008).
[35] J. D. Feick and D. Velegol, Langmuir **18**, 3454 (2002).
[36] W. Chen, S. Tan, Y. Zhou, T.-K. Ng, W. T. Ford, and P. Tong, Phys. Rev. E **79**, 041403 (2009).
[37] B. M. Mihiretie, J. C. Loudet, and B. Pouligny, J. Quant. Spectrosc. Radiat. Transfer **126**, 61 (2012).
[38] M. de Messieres, N. A. Denesyuk, and A. La Porta, Phys. Rev. E **84**, 031108 (2011).
[39] K. F. Ren, ABSPHERE (1.10) (2014); software available at https://amocops.univ-rouen.fr/en/content/download.
[40] K. F. Ren, G. Grehan, and G. Gouesbet, Opt. Commun. **108**, 343 (1994).